

# CYCLOTRON RESONANCE IN HIGH MAGNETIC FIELDS

J. KONO

*Department of Electrical and Computer Engineering, Rice University,  
Houston, Texas 77005, U.S.A.*

*E-mail: kono@rice.edu*

N. MIURA

*Institute for Solid State Physics, University of Tokyo, Kashiwa,  
Chiba 277-8581, Japan*

*E-mail: miura@issp.u-tokyo.ac.jp*

We review recent cyclotron resonance studies of semiconductors performed in high magnetic fields. This traditional semiconductor characterization method has been used to study some of the recently-developed materials systems, including ferromagnetic III-V semiconductors and two-dimensional electron gases formed in InSb/InAlSb and GaN/AlGaN heterostructures. These studies have not only provided an insight into the basic properties of these technologically-important materials but also revealed new types of splittings that can shed light on carrier-interaction effects on cyclotron resonance. In addition, we discuss new aspects of spin-split cyclotron resonance in electron systems with large spin splittings such as InAs/AlAs and InAs/GaSb as well as the polaron cyclotron resonance in II-VI compounds in megagauss magnetic fields. Finally, some of the new future directions employing far-infrared magneto-optical spectroscopy are mentioned.

## 1 Introduction

Since the first observation of cyclotron resonance (CR) in germanium and silicon in the early 1950s<sup>1-3</sup>, the methods of far-infrared (FIR) and microwave magneto-optical spectroscopy [in the terahertz (THz) and gigahertz (GHz) frequency ranges] have been used for a variety of purposes — e.g. for determining band parameters of semiconductors, elucidating carrier scattering mechanisms, studying the internal energy structure of donors and excitons, understanding the effect of carrier-phonon interactions on effective masses, and probing carrier-carrier interaction effects, especially in quantum-confined structures.

There are certain characteristics of magneto-optical spectroscopy<sup>4-11</sup> that make it a particularly powerful experimental tool for investigating electronic properties of solids. First, magnetic fields primarily couple with the electrons; their effects on the lattice are negligible in typical experimental situations (except for their indirect coupling with phonons via electrons). Thus, magneto-optical properties of solids are predominantly determined by the orbital and spin dynamics of electrons with characteristic energies  $\hbar\omega_c = eB/m^*$  and  $\hbar\omega_s = g^*\mu_B B$ , respectively, where  $\hbar$  is the Planck constant,  $\omega_c$  is the cyclotron frequency,  $m^*$  is the effective mass,  $g^*$  is the effective  $g$ -factor, and  $\mu_B$  is the Bohr magneton. Second, dynamical (or finite frequency) response contains valuable information on the states and dynamics of carriers that are not obtainable by DC transport methods. In particular, the dynamic conductivity,  $\sigma(\omega)$ , deviates from the classical Drude formula  $\sigma(\omega) = \sigma_0/(1 - i\omega\tau)$  whenever interactions and disorder are important. Many-body effects can affect the temperature and magnetic field dependences of the conductivity  $\sigma(\omega, T, B)$ , sometimes in very specific ways, making this a very useful method for comparing with theoretical calculations.

Methodologically, one can employ one of the following combinations of sources and magnets to perform high-field CR at present: i) FTIR + DC Fields — a Fourier-transform infrared (FTIR) spectrometer can be combined with a DC magnet to perform frequency-dependent spectroscopy at fixed fields; ii) CW FIR Laser + DC Fields — a CW FIR laser (e.g. a quantum-cascade laser) can be combined with a DC magnet<sup>12</sup> to perform field-dependent spectroscopy at a fixed photon energy with a high spectral resolution; iii) CW or Long Pulse FIR Laser + Pulsed Fields — a CW or long pulse FIR laser can be combined with a pulsed magnet to perform ultrahigh-field CR up to the megagauss range<sup>13</sup>; iv) Pulsed FIR Laser + DC Fields — a pulsed FIR laser (such as a free-electron laser) can be combined with a DC magnet to perform time-resolved<sup>14–16</sup> and nonlinear<sup>17,18</sup> CR experiments; v) Optically-Detected CR — photoluminescence can be used to detect CR with extremely high sensitivity<sup>19</sup>; and vi) TDTS + DC Fields — recently-developed coherent Time-Domain THz Spectroscopy (TDTS) techniques can be combined with a DC magnet<sup>20</sup> to perform measurements of complex magneto-conductivity tensors.

In the last few decades, progress in experimental techniques for high fields has opened up many new possibilities in CR research. The present state of the art of high field technology is reviewed in Vol. 1 of this book series. The strong quantization of electron energy states in high fields brings about various novel regimes. In this Chapter, particular emphasis is placed on the use of pulsed magnets [method iii) above]. They can produce much higher fields than those producible by superconducting magnets or water-cooled magnets. The highest fields generated by pulsed magnets are higher than 70 T<sup>21</sup>. If we allow the destruction of the magnets, we can generate fields well above 100 T either by the electromagnetic flux compression method<sup>22</sup> or the single-turn coil technique<sup>23–25</sup>. These *megagauss* fields have been successfully applied to many different kinds of experiments<sup>13</sup>. Megagauss CR experiments were first performed by Herlach *et al.* using the single-turn coil technique<sup>26</sup> and later by Miura *et al.* by using the electromagnetic flux compression method<sup>27</sup>.

In megagauss fields, the quantum limit is achieved in most cases, so that information on the lowest few Landau levels is obtained. A variety of physical phenomena have been investigated using megagauss CR, including resonant polaron effects in II-VI compounds<sup>28</sup>, field-induced structural phase transitions<sup>29</sup>, a semimetal-semiconductor transition<sup>30</sup>, electron-electron interaction effects<sup>31</sup>, spin-relaxation phenomena<sup>31</sup>, and a new type of combined cyclotron resonance<sup>32</sup>. Furthermore, CR experiments are possible even for “dirty” or low mobility samples, such as diamond<sup>33</sup> or diluted magnetic semiconductors<sup>34</sup>, since the condition  $\omega_c\tau > 1$  can be readily achieved in megagauss fields.

In the following sections, we review some of the latest progress in this traditional and rich field of research. First, CR has been recently observed in novel materials such as Mn-doped III-V ferromagnetic semiconductors<sup>35–39</sup>, GaN/AlGa<sup>40</sup>, and InSb/InAlSb<sup>41</sup>. These studies have not only successfully determined band parameters of these technologically-important materials but also revealed phenomena that are indicative of carrier-interaction effects. Moreover, we will describe some new aspects of *non-equilibrium* spin-split CR in InAs/AlSb quantum wells as well as resonant polaron effects in II-VI semiconductors in megagauss magnetic fields. Finally, we will summarize recent activities and future directions in the THz/FIR magneto-spectroscopy of semiconductors in high magnetic fields.

## 2 Cyclotron Resonance in InMnAs

As a first example to show the power and usefulness of ultrahigh-field CR, here we describe a series of recent CR experiments on InMnAs films and heterostructures using the single-turn coil method. InMnAs is the first-grown III-V dilute magnetic semiconductor (DMS) <sup>42,43,44</sup> and serves as a prototype for implementing electron and hole spin degrees of freedom in semiconductor devices. The carrier-induced nature of ferromagnetism in these systems opens up novel device possibilities. Indeed, recent experiments have demonstrated the feasibility of controlling ferromagnetism in these systems optically <sup>45,46,47</sup> and electrically <sup>48,49</sup>. On the other hand, the microscopic mechanism of carrier-induced ferromagnetism is not fully understood. One of the unanswered questions is the nature of the carriers, i.e. whether they are in the impurity band (*d*-like), the delocalized valence bands (*p*-like), or some type of mixed states. Since CR directly provides the effective masses and scattering times of carriers, it is an ideal method for providing an answer to this question.

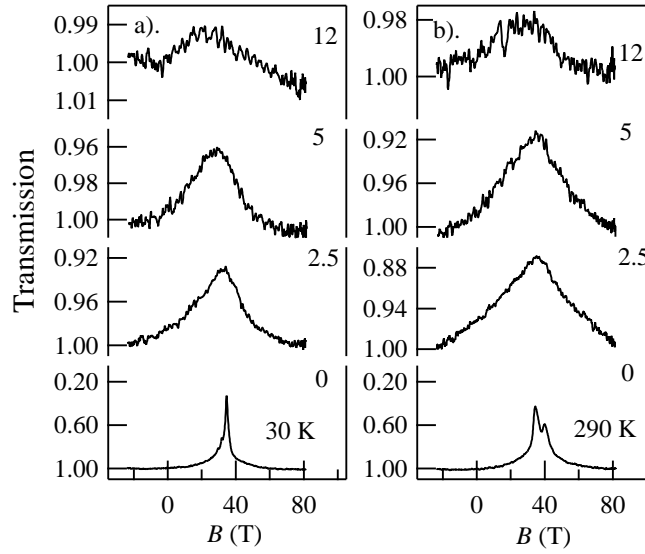


Figure 1: Experimental CR spectra for *n*-type InMnAs films with different Mn contents *x* taken at (a) 290 and (b) 30 K. The wavelength of the laser was 10.6  $\mu\text{m}$ . The resonance position shifts to lower magnetic fields with increasing *x* [from Zudov *et al.* <sup>35</sup>].

The localized Mn spins influence the delocalized conduction and valence band states through the *s-d* and *p-d* exchange interactions. These interactions are parameterized as  $\alpha$  and  $\beta$ , respectively <sup>50</sup>. Determining these parameters is important for understanding the nature of Mn states and their mixing with delocalized states. In narrow gap semiconductors like InMnAs, due to strong interband mixing,  $\alpha$  and  $\beta$  can influence *both* the conduction and valence bands and the coupling to the Mn spins does not effect all Landau levels by the same amount. As a result, CR peaks can shift as a function of *x*, the Mn concentration. This can be a sensitive method for estimating these exchange parameters.

Below we describe a series of CR experiments on InMnAs films and heterostructures<sup>35–39</sup>. These experiments clearly revealed electron and hole CR that are describable in terms of effective-mass theory, demonstrating the existence of delocalized *p*-like carriers. In addition, the observed resonances were strongly temperature-dependent, showing an abrupt reduction in width with a concomitant decrease in resonance field above the Curie temperature  $T_c$ . An 8-band  $\mathbf{k} \cdot \mathbf{p}$  theory, including full valence band complexities and treating ferromagnetism within a mean-field approximation, can show that the temperature-dependent CR peak shift is a direct measure of the carrier-Mn exchange interaction.

Various types of InMnAs samples were studied in these experiments, including *n*- and *p*-type InMnAs epitaxial layers on GaAs and *p*-type InMnAs/GaSb heterostructures. All the samples were grown by low-temperature molecular beam epitaxy (MBE)<sup>42</sup> on semi-insulating GaAs substrates. First, four *n*-type  $\sim 2\text{-}\mu\text{m}$ -thick  $\text{In}_{1-x}\text{Mn}_x\text{As}$  films with  $x = 0, 0.025, 0.050$  and  $0.120$  grown at  $200^\circ\text{C}$  were studied by Zudov *et al.*<sup>35</sup> These *n*-type films did not show ferromagnetism down to 1.5 K. Next, six *p*-type  $\sim 1\text{-}\mu\text{m}$ -thick  $\text{In}_{1-x}\text{Mn}_x\text{As}$  films with  $x = 0, 0.003, 0.0045, 0.006, 0.02$ , and  $0.025$  were studied by Matsuda *et al.*<sup>36</sup>. These *p*-type films were ferromagnetic only at very low temperatures ( $T < 10$  K). Finally,  $\text{In}_{1-x}\text{Mn}_x\text{As}/\text{Al}_y\text{Ga}_{1-y}\text{Sb}$  single heterostructures containing high densities ( $\sim 10^{19}\text{ cm}^{-3}$ ) were studied by Khodaparast *et al.*<sup>39</sup>. Unlike the *n*- and *p*-type films, these heterostructure samples showed ferromagnetism with typical Curie temperature ( $T_c$ )  $\approx 30\text{--}50$  K.

### 2.1 Electron CR in *n*-type InMnAs Films

Typical electron CR spectra measured by Zudov *et al.* for *n*-type films at 30 K and 290 K are shown in Figs. 1(a) and 1(b), respectively<sup>35</sup>. Each figure shows spectra for all four samples labeled by the corresponding Mn compositions from 0 to 12 %. All the samples show pronounced absorption peaks and the resonance field *decreases* with increasing  $x$ . Increasing  $x$  from 0 to 12% results in a  $\sim 25$  % decrease in cyclotron mass. It is important to note that at resonance only the lowest Landau level for each spin type is occupied (see Fig. 2). Thus, all the electrons were in the lowest Landau level for a given spin even at room temperature, precluding any density-dependent mass due to nonparabolicity (expected at zero or low magnetic fields) as the cause of the observed trend.

At high temperatures [e.g. Fig. 1(b)], the  $x = 0$  sample clearly shows non-parabolicity-induced spin-splitting with the weaker (stronger) peak originating from the lowest spin-down (spin-up) Landau level, while the other three samples do not show such splitting. The reason for the absence of splitting in the Mn-doped samples is a combination of 1) their low mobilities (which lead to substantial broadening) and 2) the large effective *g*-factors due to the Mn ions; especially in samples with large  $x$  only the spin-down level is substantially thermally populated (cf. Fig. 2).

Sanders *et al.*<sup>37,35,38</sup> calculated the conduction band Landau levels based on a modified Pidgeon–Brown model including full  $k_z$  dependence and *sp-d* exchange coupling. This is an eight-band  $\mathbf{k} \cdot \mathbf{p}$  method with a magnetic field along the [001] direction. A standard set of band parameters for InAs<sup>51</sup> was used, neglecting any  $x$ -dependence of these parameters. The gap was varied with the temperature according to  $E_g(T) = 0.417 - 0.000276T^2/(93+T)\text{eV}$ <sup>51</sup>. A photoemission experiment<sup>52</sup> reports  $\beta = -0.7$  eV, and a theoretical estimate<sup>53</sup> suggests

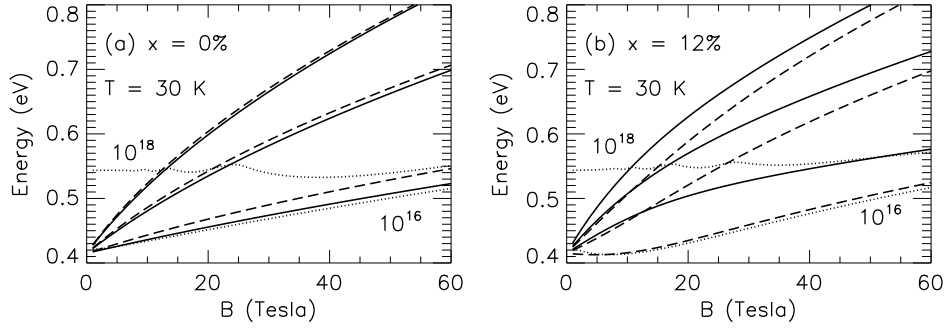


Figure 2: Electron Landau levels for  $\text{In}_{1-x}\text{Mn}_x\text{As}$  as a function of magnetic field,  $B$ , at 30 K for (a)  $x = 0$  and (b)  $x = 0.12$ . Spin up (down) levels are shown as solid (dashed) lines. The Fermi levels are indicated by dotted lines for electron concentrations of  $10^{16}$  and  $10^{18}$  cm $^{-3}$ .

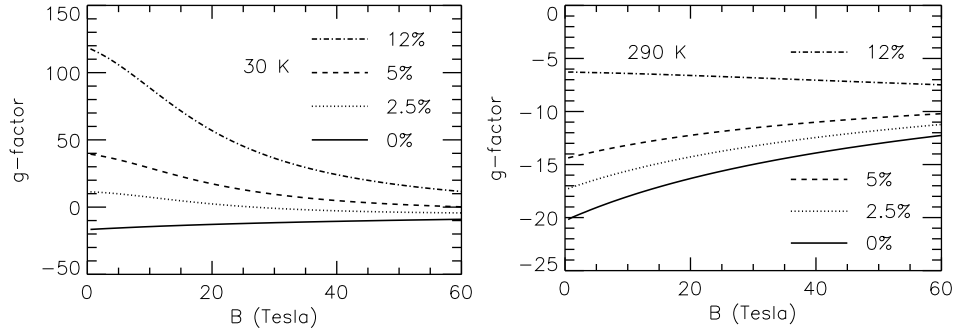


Figure 3: Electron effective  $g$  factors for  $\text{In}_{1-x}\text{Mn}_x\text{As}$  as a function of applied magnetic field for several values of  $x$ . The left and right panels correspond to  $T = 30$  K and  $T = 290$  K, respectively.

that  $\beta \approx -0.98$  eV. Here,  $\beta = -1.0$  eV and  $\alpha = 0.5$  eV were chosen as the values which best represent the observed trends (Fig. 1). Figures 2(a) and 2(b) show the lowest three Landau levels for the  $x = 0$  and 0.12 samples together with the Fermi levels (dotted lines) for carrier densities of  $10^{18}$  cm $^{-3}$  and  $10^{16}$  cm $^{-3}$ . Both the mass and  $g$ -factor are strongly energy- and magnetic field-dependent as well as  $x$ -dependent. It is also seen that in the  $x = 0.12$  sample the *spin order is reversed* and the spin splitting is significantly enhanced by the presence of Mn ions; the latter explains the absence of CR spin splitting in the  $x = 0.12$  sample. Both the sign and values of  $\alpha$  and  $\beta$  were critically important in explaining the experimental data and therefore it is a good method for determining these parameters. In Fig. 3, calculated effective  $g$ -factors are shown for the lowest Landau level as a function of magnetic field for different  $x$ . At 30 K and high  $x$ , the  $g$ -factor is extremely large ( $> 100$ ) and has the sign opposite to that of the undoped sample.

CR spectra calculated for the four  $n$ -type samples at 30 K and 290 K are shown in Figs. 4(a) and 4(b). Here, the calculated absorption coefficient for electron-active circularly polarized  $10.6$   $\mu\text{m}$  light in the Faraday configuration is plotted as a function of magnetic field at 30 K and 290 K, respectively. In the calculation, the curves were broadened based

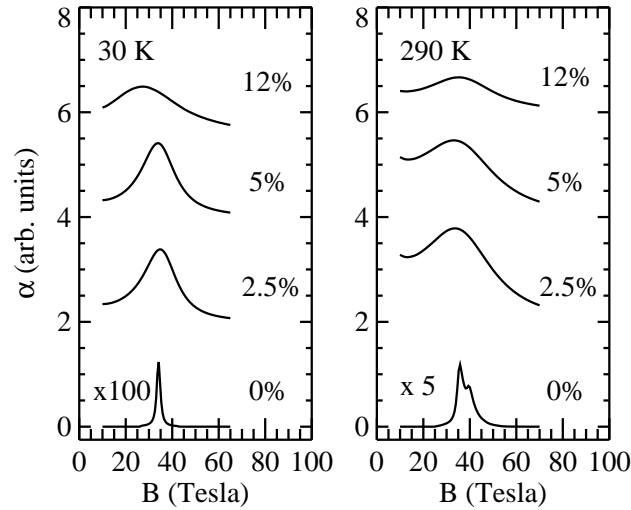


Figure 4: Calculated CR absorption as a function of magnetic field for  $n$ -InMnAs films at (a) 30 K and (b) 290 K. The curves were broadened based on the mobilities determined through Hall measurements.

on the mobilities of the samples. At 30 K, we see a shift in the CR peak as a function of doping in agreement with Fig. 1(a). For  $T = 290$  K, we see the presence of two peaks in the pure InAs sample. The second peak originates from the thermal population of the lowest spin-down Landau level (cf. Fig. 2). The peak does not shift as much with doping as it did at low temperature. This results from the temperature-dependence of the average Mn spin.

## 2.2 Hole CR in $p$ -type InMnAs Films

Typical room-temperature magneto-transmission spectra at  $10.6 \mu\text{m}$  ( $\hbar\omega = 0.224$  eV) and  $5.32 \mu\text{m}$  ( $\hbar\omega = 0.117$  eV) measured by Matsuda *et al.*<sup>36</sup> for the  $p$ -type films with different Mn concentrations are shown in Figs. 5(a) and 5(b). For all samples, a broad absorption peak is observed at  $\sim 40$  T for  $10.6 \mu\text{m}$  and at  $80$ - $100$  T for  $5.53 \mu\text{m}$ . Based on detailed theoretical analyses (discussed below), Matsuda *et al.* attributed this peak to heavy hole (HH) CR. Another absorption band is observed at  $\sim 150$  T with  $10.6 \mu\text{m}$  radiation, and is attributed to light hole (LH) CR. The cyclotron masses and cyclotron mobilities of HH were deduced from the peak positions and widths, respectively, and plotted in Fig. 6. Only the transition between Landau levels with small indices (quantum numbers) contributes to the CR even at room temperature due to the large cyclotron energy at high fields in the megagauss range. Thus, the obtained masses are significantly smaller than the band edge HH mass ( $0.35m_0$ ) due to the well known quantum effect in high magnetic fields.

As shown in Fig. 6(a), the HH cyclotron mass tends to decrease with  $x$  up to  $x = 0.02$  when measured at  $5.53 \mu\text{m}$ . However, the HH mass for the  $x = 0.025$  sample apparently deviates from this tendency. In addition, the HH mass obtained at  $10.6 \mu\text{m}$  does not show any obvious dependence on the Mn concentration. It may suggest that some other effects such as strain and disorder are playing a role in determining the masses.

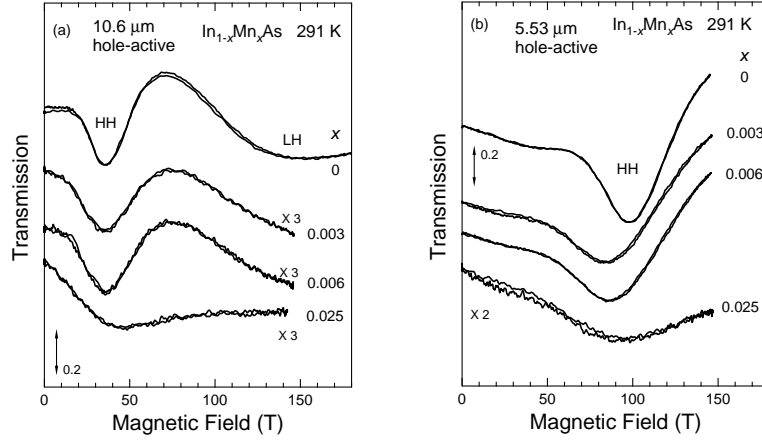


Figure 5: Room temperature cyclotron resonance spectra for  $p$ -type  $\text{In}_{1-x}\text{Mn}_x\text{As}$  with various  $x$  taken with hole-active circularly-polarized (a)  $10.6\ \mu\text{m}$  and (b)  $5.53\ \mu\text{m}$  radiation [from Matsuda *et al.* <sup>36</sup>].

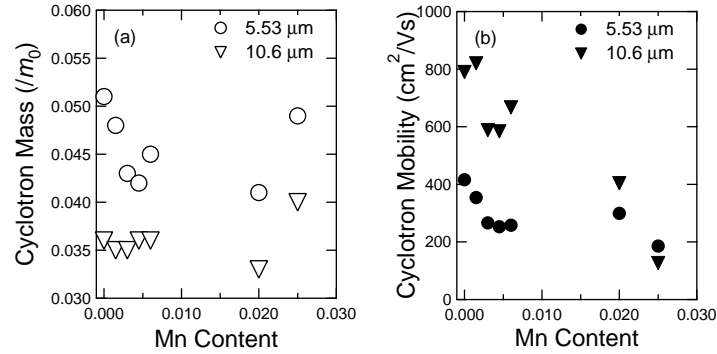


Figure 6: Deduced cyclotron masses (a) and cyclotron mobilities (b) at 291 K as functions of Mn content,  $x$ , for  $p$ -type  $\text{InMnAs}$  films [from Matsuda *et al.* <sup>36</sup>].

CR spectra for the  $x = 0.006$  and  $x = 0.025$  samples at various temperatures are shown in Figs. 7(a) and 7(b), respectively. The HH CR peak position is found to be rather insensitive to the temperature in both samples, suggesting that any effect of temperature-dependent exchange splitting of the Landau levels is small. This is because the Mn concentration is small and the relative energy of the exchange splitting to the cyclotron energy is small in the megagauss range. It should be noted that a new broad absorption band appears at low temperature and low fields below 20 T for both samples, Labeled ‘ $\alpha$ ’ in Fig. 7. One of the possible origins of this band is impurity shifted CR (ICR) absorption. If this is the case, it could be closely related to the Mn impurity band and useful for clarifying the picture of ferromagnetism. However, our CR experiments at higher photon energies (e.g.  $3.39\ \mu\text{m}$  or  $366\ \text{meV}$ ) <sup>36</sup> and theoretical calculations indicate that this is not the case.

Hole Landau levels and inter-Landau-level transitions are complicated at high fields due to wave function mixing. Figure 8 shows the calculated Landau levels at  $k_z = 0$  as a function

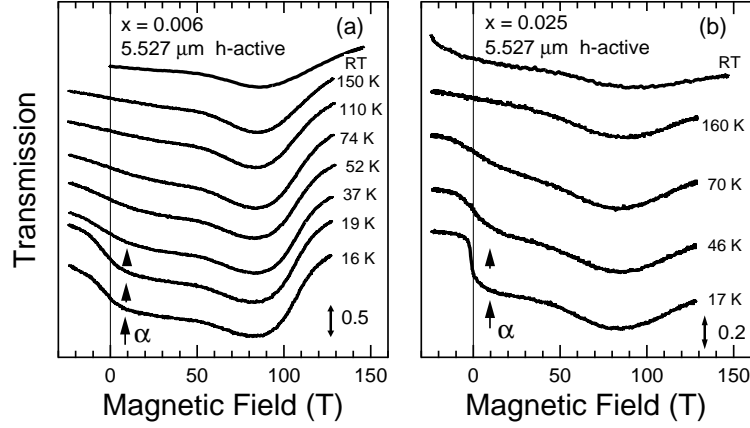


Figure 7: Temperature-dependent cyclotron resonance traces for  $p$ -type  $\text{In}_{1-x}\text{Mn}_x\text{As}$  films with (a)  $x = 0.006$  and (b)  $x = 0.025$ . A new absorption band, labeled  $\alpha$ , appears at low temperatures.

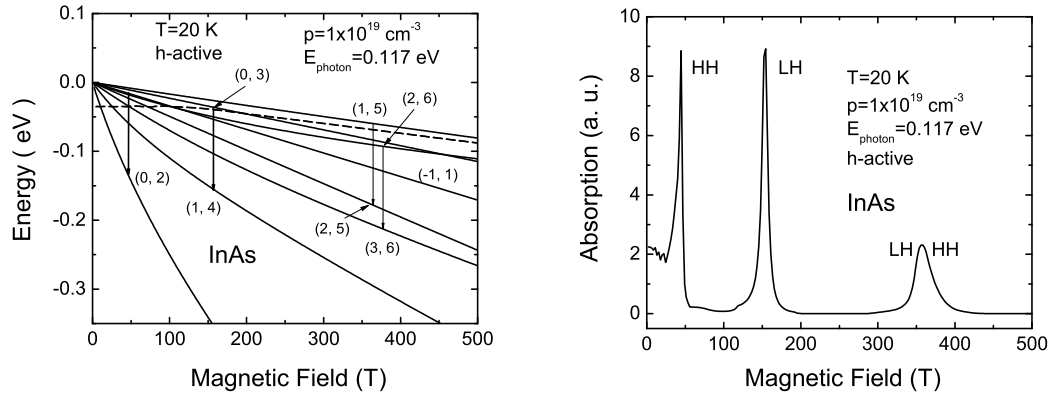


Figure 8: Calculated Landau levels of the valence band at  $\Gamma$  point and CR absorption as functions of magnetic field for  $x = 0$  at 20 K. The Fermi energy corresponding to the hole concentration  $1 \times 10^{19} \text{ cm}^{-3}$  is also shown as the dashed line. The right panel shows the CR spectrum which corresponds to the inter-Landau level transitions shown in the left panel.

of magnetic field for  $x = 0$  at 20 K. The Fermi energy corresponding to a hole concentration of  $1 \times 10^{19} \text{ cm}^{-3}$  is also indicated. Each level is specified by the notation  $(n, m)$ , where  $n$  is the manifold index ( $n = -1, 0, 1, \dots$ ) and  $m$  denotes the state within the manifold (up to eight states for manifolds  $n = 2$  and higher). Standard Luttinger parameters for InAs were used together with  $\beta = -1.0 \text{ eV}$  and  $\alpha = 0.5 \text{ eV}$ , as in the  $n$ -type case. Allowed optical transitions for hole-active polarization and a laser energy of  $0.117 \text{ eV}$  are shown in the right panel. Analysis of the wave functions for the first transition ( $\approx 50 \text{ T}$ ) show that this corresponds to a transition between the two lowest spin down HH Landau levels (i.e. the dominant components of the wavefunctions are HH spin down). The next highest transition ( $\approx 150 \text{ T}$ ) occurs between the two lowest spin down LH Landau levels. We note that for low fields below  $50 \text{ T}$  there is absorption, though not any peak structure. This



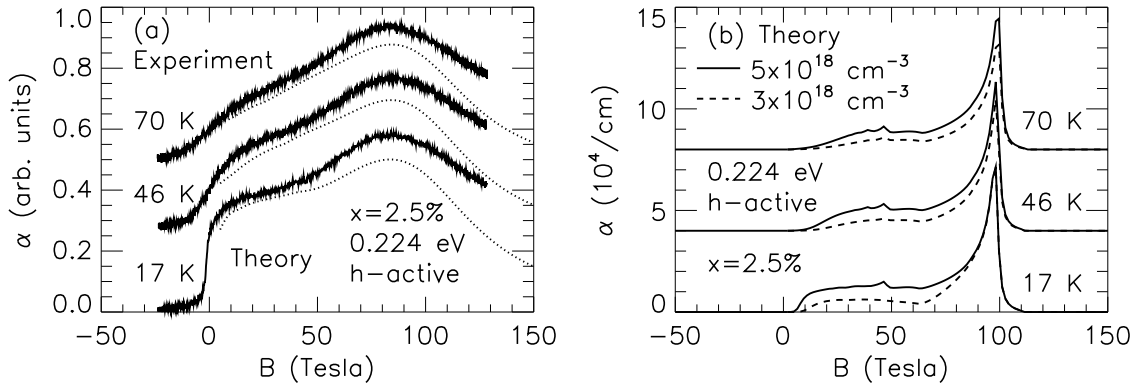


Figure 9: (a) Experimental (solid lines) and theoretical (dotted lines) hole-active CR absorption for  $\hbar\omega = 0.224$  eV versus magnetic field in  $p\text{-In}_{0.975}\text{Mn}_{0.025}\text{As}$  at 17, 46 and 70 K. The theoretical curves have FWHM linewidths of 120 meV and  $p = 5 \times 10^{18} \text{ cm}^{-3}$ . (b) Theoretical absorption spectra as in (a) with FWHM linewidths of 4 meV and  $p = 3 \times 10^{18} \text{ cm}^{-3}$  and  $p = 5 \times 10^{18} \text{ cm}^{-3}$ .

corresponds to transitions from the many higher order Landau levels lying below the Fermi energy at low magnetic fields, which can explain the feature  $\alpha$  in Fig. 7.

To illustrate this point further, Fig. 9(a) shows experimental CR spectra for the three temperatures and the corresponding theoretical CR absorption spectra are shown as dotted lines. In the theory curves in Fig. 9(a), the FWHM linewidths are taken to be 120 meV and the hole concentration is taken to be  $5 \times 10^{18} \text{ cm}^{-3}$ . In Fig. 9(b), the FWHM linewidths were reduced to 4 meV and the hole concentration was  $3 \times 10^{18} \text{ cm}^{-3}$  and  $5 \times 10^{18} \text{ cm}^{-3}$ . A HH CR transition is seen at a resonance field around 80 T. The resonance field is insensitive to temperature and the lineshape is strongly asymmetric with a broad tail at low fields. However, the width of the low field tail depends on the free hole concentration as seen in Fig. 9(b). This low field tail results from higher order Landau levels being populated, and thus, it is a sensitive measurement of the carrier density. In addition, the sharpness of the low field cutoff is seen to depend on temperature and can be attributed to the sharpness of the Fermi distribution at low temperatures.

### 2.3 Effects of Ferromagnetism on Hole CR in InMnAs/GaSb Heterostructures

Figure 10 shows CR spectra for an  $\text{In}_{0.91}\text{Mn}_{0.09}\text{As}/\text{GaSb}$  sample ( $T_c = 55$  K) at various temperatures as a function of magnetic field, reported by Khodaparast *et al.*<sup>39</sup>. From room temperature to slightly above the  $T_c$ , a broad feature (labeled ‘A’) is observed with almost no change in intensity, position, and width with decreasing temperature. However, at  $\sim 68$  K, which is still above the  $T_c$ , quite abrupt and dramatic changes are observed. First, a significant reduction in linewidth and a sudden shift to a lower  $B$  occur simultaneously. Also, it increases in intensity rapidly with decreasing temperature. In addition, a second feature (labeled ‘B’) suddenly appears at  $\sim 125$  T, which also rapidly grows in intensity with decreasing temperature and saturates, similar to feature A. Note that the temperature at which these unusual sudden CR changes occur ( $T_c^*$ ) is higher than the  $T_c$ .

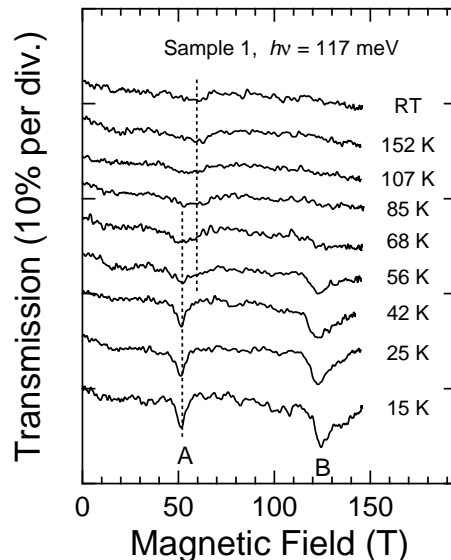


Figure 10: CR spectra for ferromagnetic InMnAs/GaSb ( $T_c = 55$  K) by Khodaparast *et al.*<sup>39</sup>. The transmission of hole-active circular polarized  $10.6 \mu\text{m}$  radiation is plotted versus magnetic field at different temperatures.

The observed unusual temperature-dependence is neither specific to this particular wavelength used nor to the sample measured. Essentially the same behavior is observed in all the samples studied. Figure 11(a) shows low-temperature CR traces for three samples at  $10.6 \mu\text{m}$ . Both features A and B are clearly observed but their intensities and linewidths vary from sample to sample. Figure 11(b) displays the wavelength-dependence of the CR spectra for one of the samples. One can see that both lines shift to higher magnetic fields with decreasing wavelength (i.e. increasing photon energy), as expected. Figures 11(c) and 11(d) show data at different temperatures for the  $T_c = 55$  K sample measured at  $9.25 \mu\text{m}$  and  $5.52 \mu\text{m}$ , respectively. The temperature-dependence observed at these shorter wavelengths is similar to what was observed at  $10.6 \mu\text{m}$ . The observations of CR with essentially the same masses in samples with different buffer layers (GaSb or AlSb) exclude the possibility of hole CR in the buffer. It was also confirmed that there was no CR in a control sample which consisted of only a GaSb layer grown on GaAs. All these facts confirm the universality of the effects we observed and their relevance to the ferromagnetic order.

The clear observation of CR indicates that *at least* a fraction of the holes are delocalized. This is in agreement with the results for the low- $T_c$   $p$ -type films, which showed similar two resonance spectra although the resonances were much broader and temperature-dependence was much weaker (see Figs. 5 and 7). However, extensive earlier attempts to observe CR in GaMnAs<sup>54</sup> did not detect any sign of resonant absorption within the magnetic field and wavelength ranges in which both light hole and heavy hole CR in GaAs were expected. This fact indicates that the holes in GaMnAs are strongly localized, that the mixing of  $p$ - and  $d$ -like states makes the effective masses of holes extremely large, or that scattering is too strong to satisfy  $\omega_c\tau > 1$ . In any case, it appears that the carriers mediating the

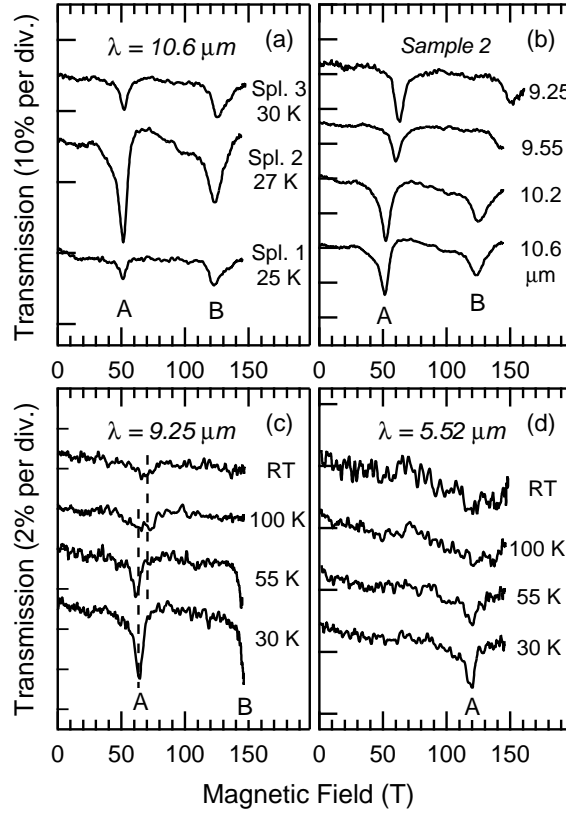


Figure 11: CR spectra for InMnAs/GaSb heterostructures: (a) sample dependence, (b) wavelength dependence (27 K), (c) temperature dependence (9.25  $\mu\text{m}$ ), and (d) temperature dependence (5.52  $\mu\text{m}$ ).

Mn-Mn exchange interaction are considerably more localized in  $\text{GnMnAs}$  than in  $\text{InMnAs}$ , consistent with recent optical conductivity<sup>55</sup> and photoemission experiments<sup>52</sup>.

In order to understand the unusual temperature dependence, Khodaparast *et al.* next considered the effects of ferromagnetism on CR spectra. They again used the developed 8-band  $\mathbf{k}\cdot\mathbf{p}$  model with  $s(p)$ - $d$  exchange interaction taken into account, and each state was specified by two indices,  $(n, \nu)$ , where  $n$  is the Landau quantum number and  $\nu$  labels the eigenvectors within each Landau manifold. Peak A in Figs. 10 and 11 can be identified as the  $\text{HH}(-1,1) \rightarrow \text{HH}(0,2)$  transition<sup>38,39</sup>. They attributed the temperature-dependent peak shift to the increase of carrier-Mn exchange interaction resulting from the increase of magnetic ordering at low temperatures. Calculated CR spectra are shown in Fig. 12(a) for bulk  $\text{In}_{0.91}\text{Mn}_{0.09}\text{As}$  with only a minimal broadening of 4 meV. The figure shows the shift of peak A with decreasing temperature.

The cyclotron energy at the center of the Landau subbands is approximately given by

$$E_{CR} = -\frac{E_g}{2} + \frac{1}{4}x\langle S_z\rangle(\alpha - \beta) + \sqrt{\left[\frac{E_g}{2} - \frac{1}{4}x\langle S_z\rangle(\alpha - \beta)\right]^2 + E_p\mu_B B}, \quad (1)$$

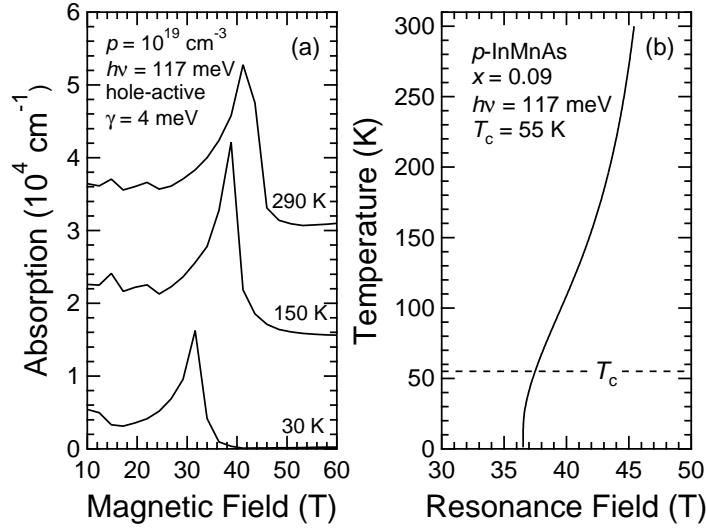


Figure 12: (a) Theoretical CR spectra for sample 1 showing a shift of peak A with temperature. (b) Calculated temperature-dependence of the resonance field for peak A.

where  $E_g$  is the energy gap,  $E_p$  is related to the Kane momentum matrix element  $P$  as  $E_p = \frac{\hbar^2 P^2}{2m_0}$ ,  $\alpha$  and  $\beta$  are  $s$ - $d$  and  $p$ - $d$  exchange constants, and  $x\langle S_z \rangle$  is the magnetization per unit cell. At high magnetic fields ( $> 40 \text{ T}$ ), the above expression can be further reduced to

$$E_{CR} \approx \frac{E_g}{2} \left( \frac{1}{\delta} - 1 \right) + \frac{1}{4} x \langle S_z \rangle (\alpha - \beta) (1 - \delta), \quad (2)$$

where  $\delta = E_g / (E_g^2 + 4E_p \mu_B B)^{1/2}$ . Assuming that the temperature-dependence of  $E_g$  and  $E_p$  is small, it follows from Eq. (2) that the peak shift should follow the temperature-dependence of  $\langle S_z \rangle$ . This shift directly measures the carrier-Mn exchange interaction. One can then calculate  $\langle S_z \rangle$  via standard mean-field theory, solving the transcendental equation

$$\langle S_z \rangle = S B_S \left( \frac{gS}{kT} \left[ \mu_B B - \frac{3kT_c \langle S_z \rangle}{gS(S+1)} \right] \right), \quad (3)$$

where  $g = 2$ ,  $B_S$  is the Brillouin function, and  $S = \frac{5}{2}$  is the spin of the magnetic ion.

The temperature-dependence of the resonance field, calculated using Eqs. (2)-(3), is presented in Fig. 12(b). Parameters used in the calculation are  $x = 0.09$ ,  $T_c = 55 \text{ K}$ ,  $E_g = 0.4 \text{ eV}$ ,  $E_p = 21 \text{ eV}$ , and  $\alpha - \beta = 1.5 \text{ eV}$ . It shows that from room temperature to 30 K the resonance field decreases by  $\sim 20\%$ , approximately the result observed in the experiment. In addition, it is seen that the shift is nonlinear with temperature and the main shift occurs at temperatures well above the  $T_c$ , which is also consistent with the experiment.

#### 2.4 CR in InMnAs — Conclusions

Electron and hole CR has been observed in  $\text{In}_{1-x}\text{Mn}_x\text{As}$ -based films and heterostructures for the first time. The main findings of these studies are: i) Owing to band mixing in this

narrow gap system, the electron CR peak actually shifts with  $x$ ; a  $\sim 25\%$  mass reduction was observed by increasing  $x$  from 0 to 0.12; ii) Theoretical calculations based on an  $8 \times 8$  band  $\mathbf{k} \cdot \mathbf{p}$  model successfully reproduce the  $x$ -dependence of electron CR peak position; iii) The  $sp-d$ , electron/hole - Mn ion exchange interactions  $\beta = -1.0$  eV and  $\alpha = 0.5$  eV were obtained as the values which best represent the observed trends; iv) At low temperatures and high  $x$ , the effective  $g$ -factor is extremely large ( $> 100$ ) and has the sign opposite to that of the  $x = 0$  sample; it is very dependent on magnetic field and is reduced substantially at high magnetic fields and temperatures; v) The clear observation of hole CR in  $p$ -type samples proves that not all of the holes are localized. The experiments are consistent with delocalized holes with the effective masses given by the band structure; vi) The mean-field approximation is adequate for the narrow gap InMnAs DMS and that the ferromagnetic transition can be understood in terms of Zener's  $p-d$  exchange interaction; vii) Hole CR has *not* been observed in ferromagnetic GaMnAs even in the megagauss range<sup>54</sup>, suggesting that the hole character may be different in InMnAs and GaMnAs.

### 3 Spin-Split Cyclotron Resonance

It is well known that cyclotron resonance exhibits nonparabolicity-induced splittings in high magnetic fields, especially in narrow gap semiconductors such as InSb or InAs<sup>27</sup>. The splitting we are concerned with in this section is due to the difference in  $g$ -factor between the Landau levels caused by band non-parabolicity (often referred to as the “ $\Delta g$  splitting”). We show how spin-split CR can be used cleverly for probing dynamics, electron-electron interactions, and Landau-level subband coupling.

#### 3.1 Spin-Split CR in Bulk GaAs

GaAs is not a narrow gap semiconductor but the  $\Delta g$  splitting has been observed in high resolution cyclotron resonance measurements<sup>56,57</sup>. The  $g$ -factor of GaAs is relatively small ( $-0.44$ ) at zero magnetic field, but it increases with magnetic field and becomes positive in sufficiently high magnetic fields. In very high magnetic fields in the megagauss range, the splitting is clearly resolvable for not only the transition between the Landau levels but also between the associated donor levels, as shown in Fig. 13. Four peaks are observed, corresponding to the transition between the Landau levels (free electron cyclotron resonance) and between the donor states (impurity cyclotron resonance) for each spin direction. As the temperature is increased, the former increases at the expense of the latter.

From the peak separation, the magnetic field-dependence of the  $g$ -factor can be estimated. It was found that the peak separation was much larger than expected from the ordinary three-level model of the energy band structure considering the  $\mathbf{k} \cdot \mathbf{p}$  interaction among the  $\Gamma_6$  conduction band, the  $\Gamma_8$  valence band, and the  $\Gamma_7$  split-off valence band. The three-level model can explain well the non-parabolicity of the conduction and valence bands in narrow-gap semiconductors such as InSb and InAs. In the case of GaAs, whose energy band is larger than these narrow gap semiconductors, it was found that a five-band model including the higher-lying conduction bands  $\Gamma_{7c}$  and  $\Gamma_{8c}$  in addition to the three

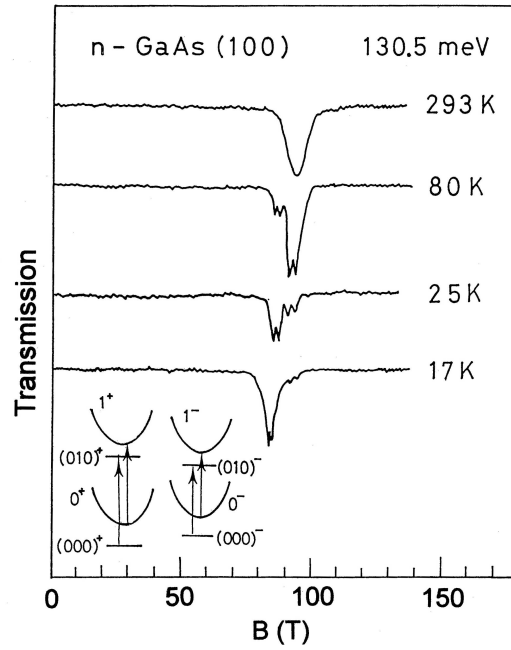


Figure 13: Cyclotron resonance in the conduction band of bulk GaAs (LPE-grown). The carrier concentration of the sample is  $1.5 \times 10^{16} \text{ cm}^{-3}$  and the thickness is  $10 \text{ }\mu\text{m}$ . The wavelength is  $9.50 \text{ }\mu\text{m}$  ( $\hbar\omega = 130.5 \text{ meV}$ ). The inset shows a schematic energy diagram of the Landau levels and donor states with two spin directions and the optical transitions between them [from Najida *et al.* <sup>58</sup>].

levels mentioned above is necessary. Good agreement was obtained between experiment and theory on the magnetic field dependence of the  $g$ -factor and spin-splitting <sup>58,59</sup>.

### 3.2 Non-equilibrium Effects in InAs/AlSb Quantum Wells

Spin-split CR in 2D systems exhibits a number of interesting effects. Here, we present two examples: a hysteresis effect in the cyclotron resonance in fast pulsed magnetic fields (in this subsection), and electron-electron interaction effects (in the next subsection).

Figure 14 shows CR spectra for a 15-nm InAs/AlSb quantum well taken in pulsed magnetic fields with *different peak fields* <sup>31</sup>. The experiments were performed in high magnetic fields produced by the single-turn coil technique. The pulse duration of the field was  $\sim 6 \text{ }\mu\text{s}$ . Normally, carrier scattering times are in the ps range, i.e. much shorter than the pulse duration, so that one can obtain optical spectra in thermal equilibrium. However, Fig. 14 shows that the spectrum changes depending on the maximum field. Since changing the maximum field is equivalent to changing the sweep rate, this implies that *the CR spectrum changes depending on how fast the field is swept*. There is *hysteresis* between up-sweep and down-sweep. The spectra taken on the falling slope are almost independent of the maximum field; only a single peak of the plus-spin is observed. On the traces taken in up-sweep, on the other hand, there is significant dependence on the maximum-field value. When the maximum field is limited to 55 T, only a single peak was observed in the same

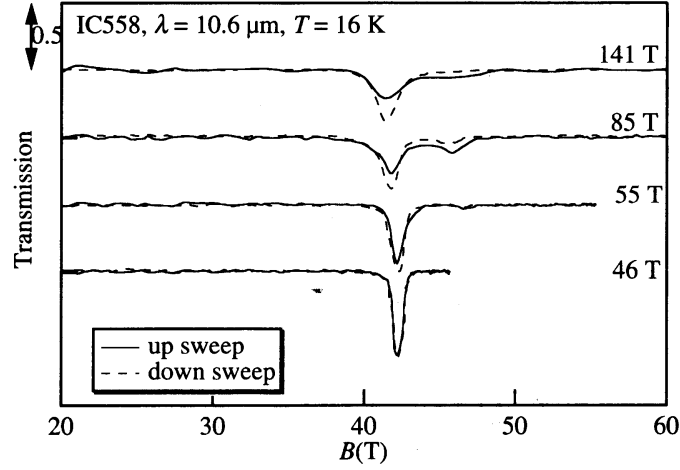


Figure 14: Cyclotron resonance in an InAs/AlSb quantum well taken with different sweeping rates. Hysteresis between up-sweep (solid lines) and down-sweep (dashed lines) becomes more pronounced as the maximum field (or equivalently the sweep rate) increases [from Arimoto *et al.*<sup>31</sup>].

way as in the down-sweep. As the maximum field of the pulse is increased to 85 T, however, the minus-spin component appears and the plus-spin component decreases. This tendency becomes more and more prominent with increasing maximum field up to 141 T. The total absorption intensity (sum of the two peak intensity) is conserved for all the spectra.

At 45 T and 16 K, the filling factor is 0.6 and the Zeeman splitting is  $\sim 23$  meV. Electrons are expected to exist only in the plus-spin state of the  $N = 0$  Landau level in equilibrium. The Boltzmann factor is  $\sim 10^{-9}$  at 16 K for the upper-spin state. Therefore, the higher spin-state CR should not be observed for equilibrium electrons. The lack of equilibrium is caused by slow spin-flip relaxation compared with the  $6 \mu\text{s}$  duration time of the magnetic field. In an up-sweep, the magnetic field increases at a rate of  $\sim 50 \text{ T}/\mu\text{s}$ , which depends on the maximum field. With  $n = 5 \times 10^{11} \text{ cm}^{-2}$ , the plus and minus-spin states of the  $N = 0$  Landau level are expected to be completely occupied in thermal equilibrium by electrons at 12.5 T, because a short inter-Landau-level relaxation time of 0.1 ns has been measured with the same sample at this field. As the field is increased, the degeneracy of the plus-spin increases and the increased levels should be filled by electrons relaxing from the minus-spin states. However, when the field increases faster than the relaxation time, some electrons will remain in the minus-spin states. Thus, the minus-spin states should be occupied by more electrons than expected for the Boltzmann distribution, resulting in a nonequilibrium population. From the sweep rate dependence of the relative peak intensity, the relaxation time from the minus spin states to the plus spin states  $\tau$  was estimated to be  $\sim 1 \mu\text{s}$ .

In InAs, the Landau level wavefunctions consist of an admixture of the up- and down-spin by the strong spin-orbit interaction, which allows the relaxation from the minus- to the plus-spin state by electric-type perturbation. Owing to the discreteness of the density of states, the spin-flip relaxation ( $\tau_1$ ) is an energy loss process and can happen through

an inelastic emission of phonons. The LO phonon energy in InAs is 29.5 meV. In fields between 12.5 T and 46 T (the resonant field of the minus-spin), where the Zeeman energy is smaller than the LO phonon energy, the LO phonon scattering is ineffective. Scattering by acoustic phonons is also unlikely, because it is difficult to satisfy the energy conservation and the momentum conservation at the same time due to the discreteness of the density of states and the large Zeeman splitting. Multi-phonon scattering may bypass the above single phonon processes<sup>60</sup>. Therefore, we can elucidate the relatively large value for the relaxation time as a process in a two-dimensional electron system.

### 3.3 *Electron–Electron Interaction Effects in InAs/(Al,Ga)Sb Quantum Wells*

Another interesting problem of spin-split CR in 2D systems is concerned with electron–electron interactions, which significantly affect temperature dependence.<sup>61–63</sup> Experiments so far have been done mostly on GaAs-based systems. The relative intensities of the two peaks do not follow the ratio of the population in the two spin states with the Boltzmann factor and the peak position shows unusual dependence on temperature and magnetic fields. This effect was found to arise from electron–electron interactions, i.e. the coupling between the two cyclotron resonance modes with different spins<sup>64,65</sup>. At first sight, it looks in contradiction with the well-known Kohn theorem that the cyclotron resonance is not affected by the interaction between electrons<sup>66</sup>. However, the theorem breaks down when different types of carriers with different effective masses co-exist.

In InAs/AlSb quantum wells, a very large effect of the mode coupling was observed by Arimoto *et al.*<sup>31</sup>. The coupling is different from the case of the GaAs system in many ways. The experiments were made in fields up to about 50 T, so that the hysteresis effects mentioned in the last subsection are not significant. Figure 15 shows cyclotron resonance spectra at different temperatures. Two peaks are observed, corresponding to spin-split CR in the lowest Landau level. The lower-field (higher-field) resonance corresponds to the plus-spin (minus-spin) CR. With varying temperature, the relative population in the two spin states changes. Band filling is larger in the plus-spin state than in the minus-spin state, so that the lower-field peak should be always larger than the upper field peak. At low temperatures ( $< 77$  K), this is the case, but the higher-field peak increases in intensity as the temperature is raised. At 195 K, the (integrated) intensities of the two peaks become almost equal and the relative integrated intensity is preserved at 300 K. Moreover, the minus spin peak has a larger line width than the plus spin peak. These experimental results are well explained by the theory of Asano and Ando<sup>65</sup> based on the exact diagonalization of a finite system. The theory is applicable for finite temperatures and also for the filling factor  $\nu > 1$ , in contrast to the theory of Cooper and Chalker<sup>64</sup>.

In contrast to the GaAs system, where similar electron–electron interaction effects were observed only at low temperatures and at small filling factor  $\nu < 1/6$ , the InAs system shows these effects at much higher temperatures and  $\nu$ . This is due to the difference in the coupling strength and the magnitude of the spin splitting between the two systems. The strength of the electron–electron interaction is proportional to a parameter  $E_c/\hbar\Delta$ , where  $E_c = \frac{e^2}{\epsilon l}$  is the Coulomb interaction,  $l$  is the magnetic length, and  $\hbar\Delta$  is the spin splitting. In InAs, the spin splitting  $\hbar\Delta$  is large, so that the coupling is smaller than in the GaAs



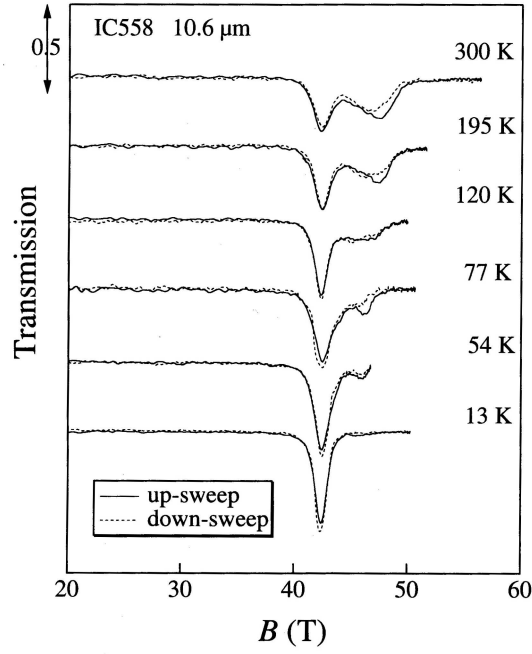


Figure 15: Cyclotron resonance spectra for an InAs/AlSb quantum well at different temperatures [from Arimoto *et al.* <sup>31</sup>].

system. In the strong coupling system as GaAs, the two peaks merge together for a large  $\nu$ , whereas in InAs, they are well resolved. Furthermore, as the spin splitting is large, the splitting is well resolved even at high temperatures where the linewidth becomes large.

Similar unusual temperature dependence has also been observed in heavily doped InAs/GaSb quantum wells. <sup>67</sup> The InAs/GaSb system is known to be a type-II quantum wells, and electrons and holes usually coexist in the structure. In heavily *n*-doped samples ( $> 10^{12} \text{ cm}^{-2}$ ), however, the electron CR is the only feature in magneto-optical spectra. Figure 16 shows CR spectra for an InAs/GaSb quantum well. The well width is 15 nm and the total electron concentration is  $3.56 \times 10^{12} \text{ cm}^{-2}$ . In this sample, not only the first sub-band but also the second subband is populated, so that four peaks are observed altogether. A surprising result is that the lowest field peak corresponding to the plus-spin transition of the first sub-band around 43 T is very weak. The tendency is more prominent as the doping is increased. Furthermore, the spin-splitting increases as the doping is increased. It should also be noticed that the peaks are shifted to the higher field side as the temperature is increased. This is in contrast to the ordinary cyclotron resonance in InAs where the effective mass should decrease as the temperature is increased due to the decrease of the band gap.

### 3.4 Spin-Mediated Subband Landau-Level Coupling in InSb/InAlSb Quantum Wells

Recently, Zhang *et al.* <sup>41</sup> observed avoided level crossings associated with the second Landau level of the ground subband and the lowest Landau level of the first excited subband

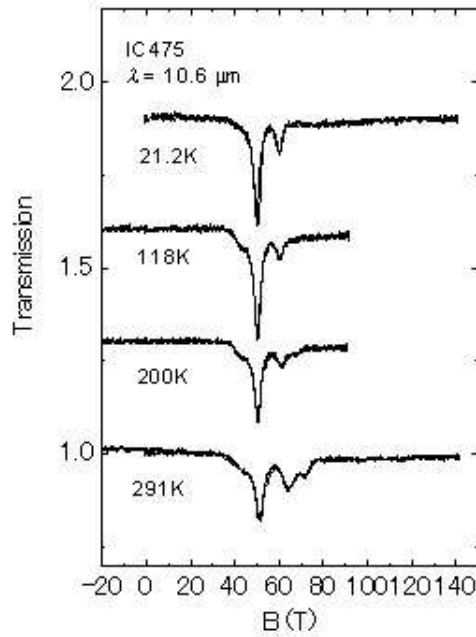


Figure 16: Cyclotron resonance in heavily doped InAs/GaSb quantum well at different temperatures. The well width is 15 nm and the carrier concentration is  $3.56 \times 10^{12} \text{ cm}^{-3}$  [from Stradling *et al.* <sup>67</sup>].

in InSb quantum wells. Using spin-resolved cyclotron resonance, they observed all four possible splittings. The energy gaps of the two anti-crossings of Landau levels with the same spin depended on the tilt of the magnetic field from the sample normal, as expected. However, anti-crossings of levels with *opposite spins*, which cannot be attributed to the same mechanism, showed gaps that were essentially tilt-angle independent.

Anti-crossing behavior was observed near the four expected crossings of the two spin-split  $n = 1$  levels of the ground subband with the two spin-split  $n = 0$  levels of the first-excited subband. Figure 17 shows this behavior at zero tilt angle, which is characterized by an intensity decay of the transitions to the lower branch of the anti-crossing and an intensity increase of transitions to the upper branch with increasing magnetic field. The energy separation of the upper and lower branch peaks when the intensities are equal is a measure of the gap energy  $\Delta E$ .

To identify the anti-crossings, the lowest Landau levels of both the ground and first-excited subbands are plotted in Fig. 18. The four crossings between the two spin levels for the ground subband  $n = 1$  Landau index and the first-excited subband  $n = 0$  Landau index are labeled 1 through 4. Crossings 1 and 4 are “spin-flip” crossings and 2 and 3 are “same spin” crossings. Four of the observed anti-crossings are identified with the predicted crossings 1 through 4. The best agreement with the predicted crossings is obtained with an intersubband energy of 59 meV. The highest-field anti-crossing for the spin-down CR, labeled “X”, can be identified as the crossing of  $(0,1,-)$  and  $(2,0,+)$ , using the notation

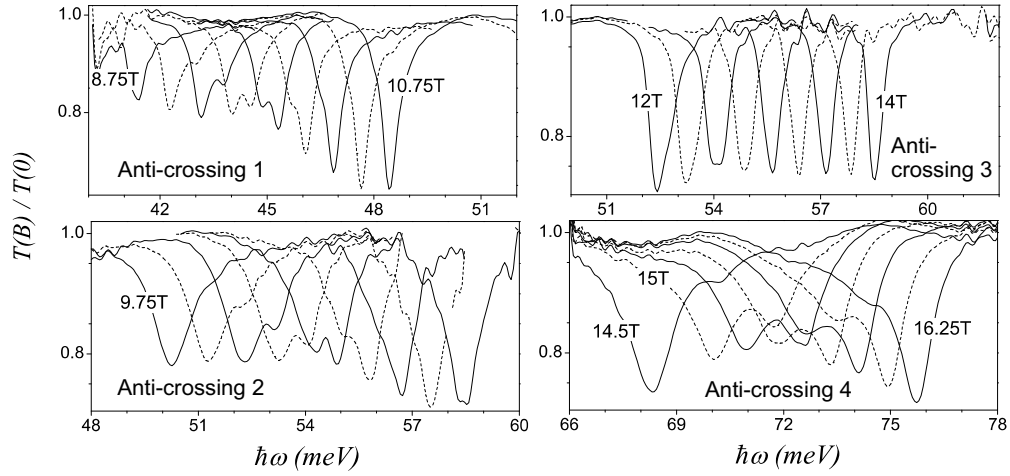


Figure 17: Cyclotron resonance spectra for an InSb/InAlSb quantum well at 4.2 K near four avoided-level crossings with a tilt angle of  $0^\circ$  [from Zhang *et al.* <sup>41</sup>].

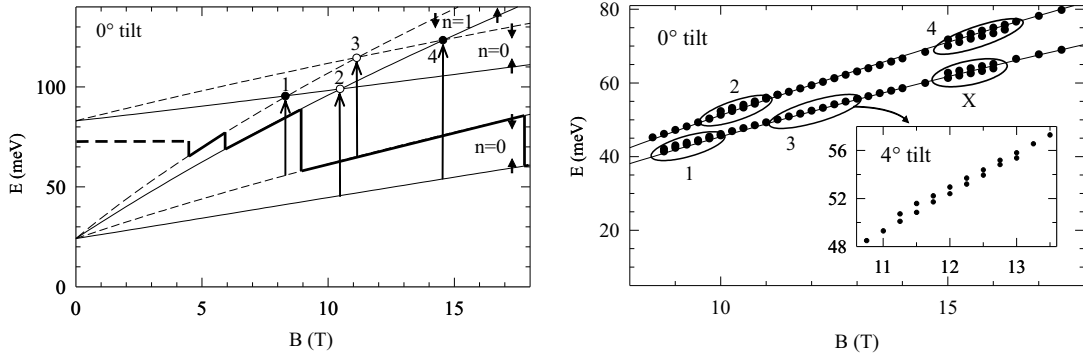


Figure 18: (Left) Calculated lowest Landau levels for the subbands  $i = 0$  and  $i = 1$ . (Right) Observed transition energies versus magnet field. The anti-crossings are labeled 1 through 4 and X. Anti-crossing 3 is shown at 4 tilt in the inset. The solid lines are the calculated energies [from Zhang *et al.* <sup>41</sup>].

$(i, n, \pm)$  where  $i$  is the subband index and  $\pm$  is spin up or down. This gives an  $i = 0$  to 2 intersubband energy of 98 meV, to be compared with the predicted value of 109 meV.

Zhang *et al.* further studied the variation of the observed anti-crossing energy gaps with tilt angle  $\theta$ . Except for anti-crossing 3, all anti-crossings exhibited a resolvable energy gap at zero tilt angle. The gaps for the “same spin” crossings, 2 and 3, increased approximately proportionally with  $\theta$ . On the other hand,  $\Delta E$  did not vary significantly for anti-crossings 4 and X, which are both “spin-flip” crossings, in the angular range studied. The proximity of anti-crossing 1 to an AlSb-like magneto-polaron feature (the LO phonon energy for AlSb is 39.7 meV) and the large  $\Delta E$  for anti-crossing 2 prevented them from determining  $\Delta E$  for anti-crossing 1 at  $\theta > 6^\circ$ . For  $\theta \leq 6^\circ$ , the gap for anti-crossing 1 was of similar size to the gaps for anti-crossings 4 and X. The insensitivity of  $\Delta E$  on tilt angle for anti-crossings 1,

4, and X is consistent with a spin-spin interaction<sup>68</sup>. Although spin-orbit effects are strong in InSb, the origin of the opposite-spin anti-crossings is not definitively identified.

## 4 Interaction of CR with Collective Excitations

Free electrons and holes interact with phonons and plasmons in semiconductors, which modify, determine, and/or renormalize their basic transport properties including effective masses. In high magnetic fields, the cyclotron energy can become resonant with such collective excitations, which can drastically change CR spectra through resonant anti-crossing behaviors. Analyzing the positions and strengths of such resonant coupling can provide quantitative information on the carrier-phonon and carrier-plasmon interactions, and there have been a large number of studies performed on a variety of bulk semiconductors<sup>8</sup>. Below, we describe recent studies of resonant electron-LO-phonon coupling in II-VI semiconductors in megagauss magnetic fields (Sec. 4.1) and the hitherto-unexplained CR splittings in various 2D electron systems (including GaN/AlGaIn<sup>40</sup>) indicative of resonant coupling of CR with an unknown collective excitation (Sec. 4.2).

### 4.1 Polaron Cyclotron Resonance in II-VI Semiconductors

In polar semiconductors such as II-VI and III-V compounds, the polaron effect is a key factor that determines the effective mass. Electrons strongly interact with LO phonons and move as polarons, which have heavier masses than the bare electrons. When  $\hbar\omega_c$  approaches the LO phonon energy  $\hbar\omega_o$  in high magnetic fields, the interaction between the electrons and LO phonons increases resonantly and a large ‘break’ appears in the magnetic field dependence of the energies of Landau levels. Since the resonant polaron effect was first observed by Dickey, Johnson, and Larsen in *n*-type InSb,<sup>69</sup> many investigations have been made on the resonant polaron effect both theoretically<sup>70–73</sup> and experimentally,<sup>56,74,75</sup> but most of the studies have been conducted on III-V compounds. Figure 19 shows a typical photon energy vs. magnetic field curve for ZnSe<sup>76</sup>. The anticrossing effect at the resonant condition  $\hbar\omega \approx \hbar\omega_o$  is clearly observed due to the large coupling constant.

The magnitude of the polaron effect is characterized by the dimensionless electron-LO phonon coupling constant  $\alpha$ . In relatively low magnetic fields, or in the low energy region, the effective mass, measured by cyclotron resonance, is the polaron mass which is larger than the bare mass  $m^*$  by a factor of about  $1 + \alpha/6$ . II-VI compounds have large values of  $\alpha$  in comparison to most III-V compounds. However, generally, the mobilities of II-VI compounds are not as high, and thus, high magnetic fields are required to observe cyclotron resonance. Furthermore, the effective masses and LO phonon energies are generally larger than in III-V compounds. Therefore, the resonant polaron effect in II-VI compounds can be studied only in very high magnetic fields in the megagauss range. At the ISSP of the University of Tokyo, systematic studies of the polaron cyclotron resonance of II-VI compounds have been performed using the megagauss magnetic fields generated by electromagnetic flux compression and the single-turn coil technique over a wide range of photon energy across the resonant polaron effect region<sup>28, 76–80</sup>.

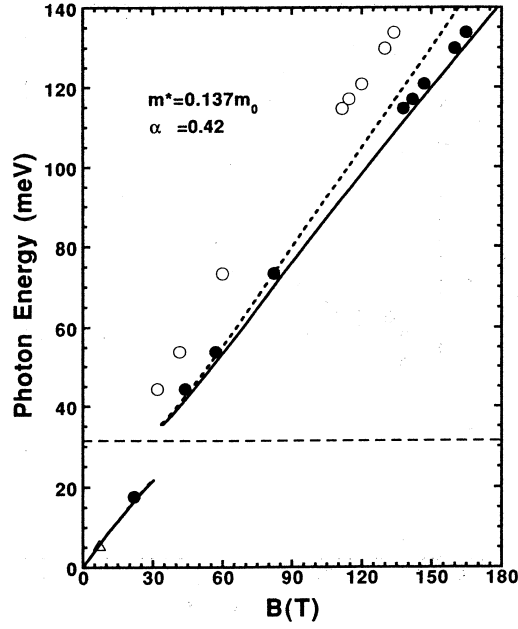


Figure 19: Plot of the photon energy of the cyclotron resonance as a function of magnetic field for ZnSe [from Imanaka *et al.*<sup>76</sup>].

The energy states of polarons in the resonant polaron region can be approximately calculated if one employs the second order perturbation method for the Fröhlich Hamiltonian as was first demonstrated by Dickey *et al.*<sup>69</sup>. The  $N = 0$  and  $N = 1$  Landau levels are represented as follows for the phonon emitting process.

$$\mathcal{E}(0) = \frac{1}{2}\hbar\omega_c - \frac{\alpha(\hbar\omega_o)^2}{2\pi^2}\mathcal{P} \int d\mathbf{k} \sum_N \frac{|\mathcal{H}'_{N0}(\mathbf{k})|^2}{(N + \frac{1}{2})\hbar\omega_c + \hbar\omega_o + \frac{\hbar^2 k_z^2}{2m^*} - \mathcal{E}(0)} \quad (4)$$

$$\mathcal{E}(1) = \frac{3}{2}\hbar\omega_c - \frac{\alpha(\hbar\omega_o)^2}{2\pi^2}\mathcal{P} \int d\mathbf{k} \sum_N \frac{|\mathcal{H}'_{N1}(\mathbf{k})|^2}{\mathcal{E}(0) + N\hbar\omega_c + \hbar\omega_o + \frac{\hbar^2 k_z^2}{2m^*} - \mathcal{E}(1)}, \quad (5)$$

where  $\mathcal{H}'_{N0}$  and  $\mathcal{H}'_{N1}$  denote the matrix element for the interaction of the  $N = 0$  and  $N = 1$  Landau levels with the  $N$ th Landau levels. By choosing proper values of  $m^*$  and  $\alpha$ , good agreement has been obtained between the experimental results and calculation for various II-VI compounds. In the calculation, band nonparabolicity needs to be taken into account since it becomes significant in the high energy region. From such comparison between experiments and calculation, one can obtain  $m^*$  and  $\alpha$  for these crystals. Table 1 lists the values of  $m^*$  and  $\alpha$  of typical II-VI compounds<sup>28</sup>.

Here,  $m^*$  is the bare band edge mass without electron-phonon interactions,  $m_p^*$  is the polaron mass observed in the low energy limit,  $m_C^*$  is the effective mass observed at a wavelength of  $10.6 \mu\text{m}$ ,  $\alpha$  is the Fröhlich coupling constant,  $\hbar\omega_o$  is the LO phonon energy, and  $B_r$  is the magnetic field where the resonant polaron coupling occurs ( $\hbar\omega = eB_r/m_p^*$ ). Thus, the polaron masses of most of the typical II-VI compounds have been determined<sup>28</sup>.

Table 1: The bare mass  $m^*$ , polaron mass  $m_p^*$  and the coupling constant  $\alpha$  in II-VI semiconductors [from Miura *et al.*<sup>28</sup>].

Material	$m^*/m_0$	$m_p^*/m_0$	$m_c^*/m_0$ (117meV)	$\alpha$	$\hbar\omega_o$ (meV)	$B_r$ (T)	Ref.
ZnO	0.25	0.290	0.265	0.97	73.0	280	79
ZnS (ZB)	0.200	0.221	0.188	0.630	43.4	54.3	81
ZnSe	0.137	0.1451	0.141	0.420	31.4	51.4	76
CdS ( $\mathbf{B} \parallel \mathbf{c}$ )	0.168	0.188	0.162	0.514	37.8	54.9	80
CdS ( $\mathbf{B} \perp \mathbf{c}$ )	0.159	0.180	0.157	0.555	37.8	51.9	80
CdSe( $\mathbf{B} \parallel \mathbf{c}$ )	0.118	0.130	0.118	0.419	26.2	26.7	28
CdTe	0.092	0.098	0.104	0.4	21.3	18.0	74, 82

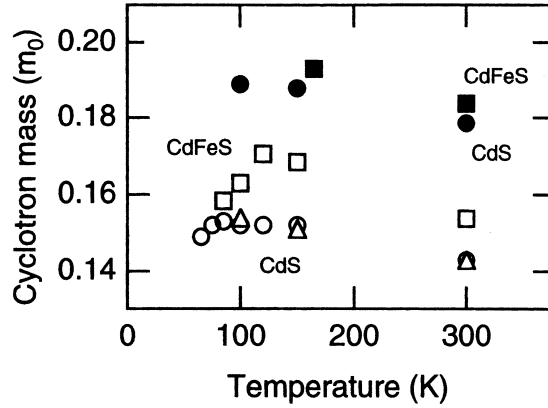
Figure 20: The temperature dependence of the effective mass determined by cyclotron resonance in CdS and  $\text{Cd}_{0.95}\text{Fe}_{0.05}\text{S}$ . Closed circles: CdS at 73.4 meV, Open circles and open triangles: CdS at 44.3 meV, Closed squares:  $\text{Cd}_{0.95}\text{Fe}_{0.05}\text{S}$  at 73.4 meV, Open squares:  $\text{Cd}_{0.95}\text{Fe}_{0.05}\text{S}$  at 44.3 meV [from Matsuda *et al.*<sup>83</sup>].

Figure 20 shows the cyclotron effective masses of CdS and  $\text{Cd}_{0.95}\text{Fe}_{0.05}\text{S}$ <sup>83</sup> as a function of temperature for two different photon energies (73.4 meV and 44.3 meV). The effective mass decreases as the photon energy is increased above the LO phonon energy in both materials, as expected from the resonant polaron effect. The effective mass decreases with the increasing temperature in the high temperature range. In particular, the effective mass determined at  $\hbar\omega = 73.4$  meV shows a prominent peak at around 120 K. The temperature dependence is more prominent in  $\text{Cd}_{1-x}\text{Fe}_x\text{S}$ . The effect in CdS was analyzed by Devreese and coworkers using the memory function approach based on the Feynman polaron model.<sup>84</sup> According to the theoretical calculation, the temperature dependence with a peak at around 120 K was well explained by taking account of the LO phonon interaction and the piezoelectric interaction as well as the impurity scattering. However, the large enhancement of the effect in  $\text{Cd}_{1-x}\text{Fe}_x\text{S}$  still remains an interesting problem to be solved in connection with the interplay between the lattice polaron and the magnetic polaron.

#### 4.2 Density-Dependent CR Splittings in 2-D Electron Gases

Some twenty years ago, Schlesinger *et al.*<sup>85</sup> observed an abrupt splitting or broadening of the CR line of a 2D electron gas (2DEG) at a GaAs/AlGaAs heterojunction. The splitting occurred in a narrow magnetic field range, reminiscent of anti-crossing behaviors seen in resonant polaron CR (Sec. 4.1), indicating a resonant interaction of the CR mode with another collective excitation in the 2DEG system. However, the critical energy at which this resonant coupling occurs was found to be dependent on the density of the 2D electrons,  $n_{2D}$ , implying that electron–electron interactions might be important. More specifically, the critical energy versus density for various samples with different densities was approximately represented by a *universal curve*, expressed by  $E_{\text{crit}} = e^2 \sqrt{n_{2D}} / \epsilon$ , where  $e$  is the electronic charge and  $\epsilon$  is the dielectric function.

Schlesinger *et al.*<sup>85</sup> proposed a model based on the interaction of CR with a non-zero-momentum ( $q \neq 0$ ) magneto-plasmon. It is, in a sense, a self-interaction effect since CR is the  $q = 0$  magneto-plasmon; it is also similar to the old idea of CR-plasmon coupling proposed and verified in bulk semiconductors.<sup>8,86</sup> However, a 2D magneto-plasmon shows a non-monotonic dispersion, exhibiting a characteristic minimum at a finite  $q$ , called a *magneto-roton* minimum, and in order for the self-interaction to occur, the depth of the roton must be large enough for the CR-roton coincidence to occur. In addition, disorder has to be large enough to couple CR to this mode to produce the observed splittings. Subsequent theoretical studies by Kallin and Halperin<sup>87</sup>, and MacDonald,<sup>88</sup> however, have shown that the roton minimum can never become smaller than the CR energy, and the observations by Schlesinger *et al.* have remained unexplained to date.

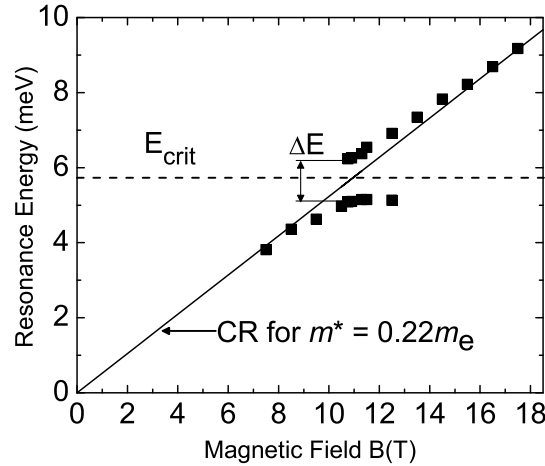


Figure 21: (Left) Far-infrared transmission for on a GaN/AlGaN 2DEG sample of density  $1.14 \times 10^{12} \text{ cm}^{-2}$  for various magnetic fields, reported by Syed *et al.*<sup>40</sup>. All data are normalized to the zero-magnetic-field transmission. Traces are offset vertically for clarity. (Right) Peak positions of transmission minima as a function of magnetic field. High and low field data follow the CR with an effective mass of  $m^* = 0.22m_0$ . Around 11 T an apparent level anti-crossing occurs with a critical energy  $E_{\text{crit}} = 5.7$  meV, with the two branches separated by a gap of  $\sim 1.2$  meV.

Recently, Syed *et al.*<sup>40</sup> observed large CR splittings in MBE-grown GaN/AlGaN heterostructures. The basic characteristics of the splittings were essentially the same as the earlier observations by Schlesinger *et al.* for GaAs/AlGaAs. The left panel of Fig. 21 shows representative data. At fields  $> 15$  T and  $< 8$  T, a single resonance is observed with an effective mass of  $m^* = 0.22m_0$ . However, at intermediate fields ( $8 \text{ T} < B < 15 \text{ T}$ ), the resonance splits into two, and the intensity of the higher-lying line gradually increases with  $B$  at the expense of the lower-lying line. The right panel of Fig. 21 shows resonance energy versus magnetic field. The solid line is a linear fit to the high and low field data. Between 10 T and 14 T, splitting is clearly visible. The two resonance branches are separated by a gap of  $\Delta E \sim 1.2 \text{ meV}$ . The mid-point of this gap resides at  $E_{\text{crit}} \sim 5.7 \text{ meV}$ . The splitting indicates a level anti-crossing between CR and some other resonance at  $\sim 5.7 \text{ meV}$ .

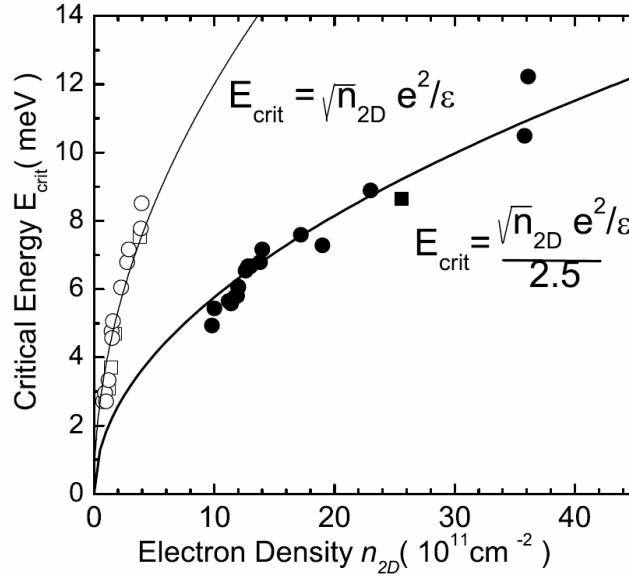


Figure 22: Critical energy versus electron density for the CR splittings observed for GaN/AlGaN by Syed *et al.*<sup>40</sup> The full square is for a GaN/AlGaN sample studied earlier by Wang *et al.*<sup>89</sup> The open circles and squares are data for Si and GaAs 2DEGs, adapted from Schlesinger *et al.*<sup>85</sup> [from Syed *et al.*<sup>90</sup>].

Figure 22 shows the dependence of  $E_{\text{crit}}$  on  $n_{2D}$ , for ten samples studied. A data point by Wang *et al.*,<sup>89</sup> is included; its position indicates that the same phenomenon is at work. As in the work by Schlesinger *et al.*, the critical energy seems to follow a  $\sqrt{n_{2D}}$  dependence. However, the exact form does not agree with the universal formula proposed by Schlesinger *et al.*, i.e.  $E_{\text{crit}} = e^2 \sqrt{n_{2D}} / \epsilon$ . Figure 22 also includes the curve containing the MOSFET and AlGaAs/GaAs data from Ref.<sup>85</sup>. While these data follow the universal behavior, the GaN data deviate from this relationship by a factor of  $\sim 2.5$ . Obvious differences in  $\epsilon$  and  $m^*$  between these materials cannot resolve the discrepancy.

The observed large CR splittings in GaN/AlGaN and their density dependence support the view that the manifestation of splittings is a universal property of 2-D electrons in



high magnetic fields. However, at this point the physical origin of this phenomenon is still elusive. In an attempt to shine some light on this problem, Syed *et al.* have recently revisited GaAs-based 2-D electrons by performing CR measurements on a variety of modulation-doped GaAs/AlGaAs structures with varying densities and mobilities<sup>90</sup>. Their aim was to find some correlation between the CR splitting and any other parameter of the samples. They carefully investigated the magnitude of the splitting  $\Delta E$  versus transport lifetime  $\tau_t$  (from mobility), quantum lifetime  $\tau_q$  (from SdH oscillations), CR lifetime  $\tau_{CR}$  (from CR linewidth), and electron density  $n_{2D}$  (from Hall and SdH measurements). There was very little correlation between  $\Delta E$  and  $n_{2D}$  or  $\tau_{CR}$ . However, there was a trend of decreasing  $\Delta E$  with increasing  $\tau_t$  and  $\tau_q$ . In particular,  $\Delta E$  was found to increase rather rapidly as  $\tau_t$  and  $\tau_q$  decreased towards zero. These results indicate that increased electron scattering somehow increases the splitting. Since increased electron scattering leads to a wider sampling range in  $q$ -space, this seems to imply that the excitation that couples to CR resides at finite momentum ( $q \neq 0$ ), such as the magneto-roton. However, at this point, there exists no convincing theoretical model that can provide a consistent and quantitative explanation for the splitting magnitude versus density.

## 5 Future Directions

There have been recent technological developments in high-field magneto-optical spectroscopy in the far-infrared or THz, which enable new classes of CR experiments. These experiments are aimed towards 1) time-resolved CR for studying carrier dynamics in Landau/Zeeman quantized systems, 2) spatially-resolved CR for studying magneto-optics in single nanostructures, and 3) nonlinear CR experiments using intense THz radiation for exploring non-perturbative nonlinear magneto-optical phenomena.

### 5.1 Time-Resolved Magneto-Spectroscopy

Time-resolved THz/FIR spectroscopies have been used recently for studying carrier dynamics in magnetic fields. These include FIR single-color pump-probe spectroscopy<sup>15</sup>, optical-pump/FIR-probe spectroscopy<sup>14,16,91</sup>, and time-domain THz spectroscopy (TDTS)<sup>92,93,20</sup>. TDTS techniques allow one to measure the amplitude and phase of the coherent THz radiation emitted by or transmitted through the sample. Shown in Fig. 23 are cyclotron oscillations observed in a high-mobility 2DEG<sup>94</sup>.

These coherent oscillations are ‘free induction decay’ in the language of coherent optics of two-level atoms or NMR, and the “two levels” here are the highest filled Landau level and the lowest unfilled Landau level. The incident THz pulse creates a coherent superposition of the two Landau levels, and, thus, a macroscopic polarization appears and starts radiating coherently. The polarization exponentially decays (decoherence or dephasing) while showing sinusoidal cyclotron oscillations. From the decay time and oscillation frequency, we can directly determine the  $T_2$  (or  $T_2^*$ ) and  $\omega_c$ , respectively. These results promise further explorations into coherent and quantum optical experiments such as “cyclotron” echo and Rabi flopping.

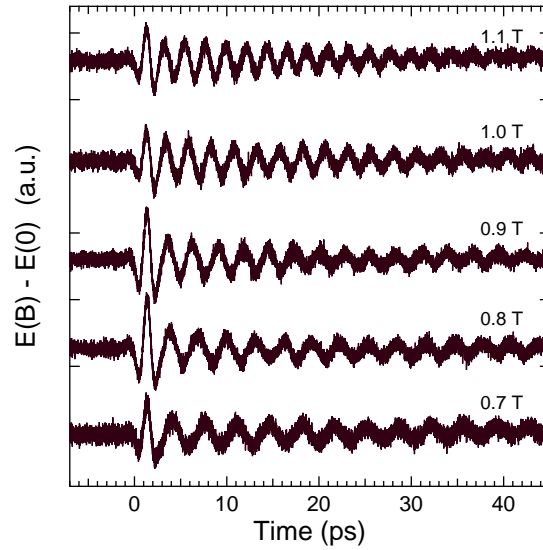


Figure 23: Coherent cyclotron oscillations in a high-mobility 2DEG [from Wang *et al.*<sup>94</sup>].

### 5.2 Optically-Detected THz Resonance Spectroscopy of Nanostructures

A new type of detection scheme, Optically-Detected THz Resonance (ODTR) spectroscopy, has been developed during the past decade<sup>95,96,97,19,98,99</sup>. In this scheme, THz resonances are detected through the change in the intensity of photoluminescence (PL) while the magnetic field is swept, rather than measuring THz absorption directly. This technique, originally developed for the microwave (GHz) region, was extended to the THz by Wright *et al.*<sup>95</sup> in studies of epitaxial GaAs, and subsequently by others. Remarkable sensitivity in comparison with conventional FIR methods have been demonstrated in studies of CR<sup>96</sup>, impurity transitions<sup>97,19</sup>, and internal transitions in excitons<sup>98,99</sup>. Since carriers are optically created, ODTR enables detection of CR in clean systems with no intentional doping with increased scattering time, and in materials for which doping is difficult. Furthermore, with ODTR it is possible to select spectrally a specific PL feature, among various band-edge features, as the detection “channel.” It is then possible to use the specificity of the THz spectrum to obtain information about recombination mechanisms and the interactions that give rise to the various lines. Lastly, and most importantly, ODTR opens up the possibility to perform THz spectroscopy of single nanostructures. The spatial resolution is determined by that of the PL probe, which can be a confocal micro-PL system or a near-field scanning optical spectroscopy system, not by the THz optics. A method for determining the spin coherence time  $T_2$  of a single electron in a single quantum dot has been recently proposed<sup>100</sup>. Experimental efforts on ODTR in single nanostructures have just begun<sup>101</sup>.

### 5.3 Nonlinear Far-Infrared Magneto-Optics

For over three decades, the use of strong laser fields to explore quantum optical phenomena has played a major role in our understanding of the interaction of light with atomic

systems. The use of lasers to investigate quantum optical analogs in condensed matter and mesoscopic systems has become an extremely active area of research over the past 15 years. Nevertheless, many of the well-known ‘strong field’ quantum optical phenomena (Rabi oscillations, Autler–Townes effect, optical gain without population inversion, electromagnetically-induced transparency, and slowing and freezing of light pulses) remain for the most part unexplored in condensed matter systems, primarily due to rapid dephasing times which plague electronic excitations and the lack of suitable lasers possessing spectral and temporal characteristics necessary to create and probe the electronic coherences on ultrafast time scales. Hydrogenic excitons<sup>102</sup> and donors<sup>103</sup> in magnetic fields in intense THz fields are an ideal system to examine nonlinear and quantum optical phenomena in solid-state systems in a well-controlled manner since the optical field dictates the discrete internal states of excitons whereas the magnetic field localizes the center-of-mass motion and tunes the internal energy levels. The large spatial extent of excitons results in strong light-matter coupling in the THz range (via, e.g.  $1s \rightarrow 2p_{\pm}$  transitions), and dramatic non-perturbative phenomena are expected<sup>104–106</sup>.

## Acknowledgments

We thank a number of collaborators who have contributed to the work described in this chapter. These include T. Ando, H. Arimoto, K. Asano, Y. Imanaka, S. Katsumoto, G. A. Khodaparast, F. V. Kyrychenko, Y. H. Matsuda, H. Munekata, G. D. Sanders, C. J. Stanton, R. A. Stradling, Y. Sun, and M. A. Zudov. We also thank Y. J. Wang and M. B. Santos for sharing their unpublished results on InSb/InAlSb quantum wells. J.K. acknowledges support from NSF through Grant Nos. DMR-0134058, DMR-0216838, DMR-0325474, and INT-0221704.

## References

1. G. Dresselhaus, A. F. Kip, and C. Kittel, *Phys. Rev.* **92**, 827 (1953).
2. B. Lax, H. J. Zeiger, R. N. Dexter, and E. S. Rosenblum, *Phys. Rev.* **93**, 1418 (1953).
3. G. Dresselhaus, A. F. Kip, and C. Kittel, *Phys. Rev.* **98**, 368 (1955).
4. B. Lax and J. G. Mavroides, “Cyclotron Resonance,” in *Solid State Physics*, edited by F. Seitz and D. Turnbull (Academic Press, New York, 1960), vol. 11, pp. 261–400.
5. E. D. Palik and J. K. Furdyna, “Infrared and Microwave Magnetoplasma Effects in Semiconductors,” *Rep. Prog. Phys.* **33**, 1193 (1970).
6. J. G. Mavroides, “Magneto-optical Properties,” in *Optical Properties of Solids*, edited by F. Abeles (North-Holland, Amsterdam, 1972), pp. 351–528.
7. B. D. McCombe and R. J. Wagner, in *Advances in Electronics and Electron Physics*, edited by L. Marton (Academic Press, New York, 1975), vol. 37, pp. 1–78.
8. B. D. McCombe and R. J. Wagner, in *Advances in Electronics and Electron Physics*, edited by L. Marton (Academic Press, New York, 1975), vol. 38, pp. 1–53.
9. A. Petrou and B. D. McCombe, in *Landau Level Spectroscopy*, edited by G. Landwehr and E. I. Rashba (Elsevier Science, Amsterdam, 1991), pp. 679–775.

10. R. J. Nicholas, in *Handbook on Semiconductors, Vol. 2 "Optical Properties"*, edited by M. Balkanski (Elsevier, Amsterdam, 1994), pp. 385–461.
11. J. Kono, "Cyclotron Resonance," in *Methods in Materials Research*, edited by E. N. Kaufmann *et al.* (John Wiley & Sons, New York, 2001), Unit 9b.2.
12. D. C. Larrabee *et al.*, *Optics Lett.* **29**, 122 (2004).
13. N. Miura, G. Kido, and F. Herlach, this book series, Vol. 1, Chap. 9.
14. J. Kono *et al.*, *Appl. Phys. Lett.* **75**, 1119 (1999).
15. B. N. Murdin *et al.*, *Phys. Rev. B* **59**, R7817 (1999).
16. G. A. Khodaparast *et al.*, *Phys. Rev. B* **67**, 035307 (2003).
17. T. A. Vaughan *et al.*, *Phys. Rev. B* **53**, 16481 (1996).
18. S. K. Singh *et al.*, *Phys. Rev. B* **58**, 7286 (1998).
19. J. Kono *et al.*, *Phys. Rev. B* **52**, R8654 (1995).
20. S. A. Crooker, *Rev. Sci. Instrum.* **73**, 3258 (2002).
21. F. Herlach and N. Miura, this book series, Vol. 1, Chap. 7.
22. Y. H. Matsuda *et al.*, *Rev. Sci. Instrum.* **73**, 4288 (2002).
23. F. Herlach and R. McBroom, *J. Phys. E: Sci. Instrum.* **6**, 652 (1973).
24. K. Nakao *et al.*, *J. Phys. E: Sci. Instrum.* **6**, 652 (1973).
25. O. Portugal *et al.*, *J. Phys. D: Appl. Phys.* **32**, 2354 (1999).
26. F. Herlach *et al.*, *Phys. Rev. B* **10**, 682 (1974).
27. N. Miura, G. Kido, and S. Chikazumi, *Solid State Commun.* **18**, 885 (1976).
28. N. Miura and Y. Imanaka, *physica status solidi (b)* **237**, 244 (2003).
29. H. Yokoi *et al.*, *J. Phys. Soc. Jpn.* **62**, 1245 (1993).
30. D. J. Barnes *et al.*, *Phys. Rev. B* **49**, 10474 (1994).
31. H. Arimoto, N. Miura, and R. A. Stradling, *Phys. Rev. B* **67**, 155319 (2003).
32. H. Yokoi *et al.*, *Proc. 20th Int. Conf. Phys. Semiconductors* (World Scientific, Singapore, 1991), p.1779.
33. J. Kono *et al.*, *Phys. Rev. B* **48**, 10917 (1993),
34. Y. H. Matsuda *et al.*, *Phys. Rev. B* **65**, 115202 (2002).
35. M. A. Zudov *et al.*, *Phys. Rev. B* **66**, 161307(R) (2002).
36. Y. H. Matsuda *et al.*, *Phys. Rev. B* **70**, 195211 (2004).
37. G. D. Sanders *et al.*, *Phys. Rev. B* **68**, 165205 (2003).
38. G. D. Sanders *et al.*, *J. Appl. Phys.* **93**, 6897 (2003).
39. G. A. Khodaparast *et al.*, *Physica E* **21**, 978 (2004); see also cond-mat/0307087.
40. S. Syed *et al.*, *Phys. Rev. B* **67**, 241304 (2003).
41. X. H. Zhang *et al.*, *AIP Conf. Proc.* 772 (2005); also submitted to *Phys. Rev. B*.
42. H. Munekata *et al.*, *Phys. Rev. Lett.* **63**, 1849 (1989).
43. H. Ohno *et al.*, *Phys. Rev. Lett.* **68**, 2664 (1992).
44. H. Munekata *et al.*, *Appl. Phys. Lett.* **63**, 2929 (1993).
45. S. Koshihara *et al.*, *Phys. Rev. Lett.* **78**, 4617 (1997).
46. A. Oiwa *et al.*, *Appl. Phys. Lett.* **78**, 518 (2001).
47. A. Oiwa *et al.*, *Phys. Rev. Lett.* **88**, 137202 (2002).
48. H. Ohno *et al.*, *Nature* **408**, 944 (2000).
49. D. Chiba *et al.*, *Science* **301**, 943 (2003).

50. J. Furdyna, *J. Appl. Phys.* **64**, R29 (1988).
51. I. Vurgaftman, J. R. Meyer, and L. R. Ram-Mohan, *J. Appl. Phys.* **89**, 5815 (2001).
52. J. Okabayashi *et al.*, *Phys. Rev. B* **65**, 161203(R) (2002).
53. T. Dietl *et al.*, *Phys. Rev. B* **63**, 195205 (2001).
54. Y. H. Matsuda *et al.*, *3rd Symp. on Phys. & Appl. of Spin-Related Phenomena in Semicond.*, 1997, pp. 42-44.
55. K. Hirakawa *et al.*, *Phys. Rev. B* **65**, 193312 (2002).
56. M. A. Hopkins *et al.*, *Phys. Rev. B* **36**, 4789 (1987).
57. H. Sigg *et al.*, *Solid State Commun.* **61**, 685 (1987).
58. S. P. Najda *et al.*, *Phys. Rev. B* **40**, 6189 (1989).
59. N. Miura, H. Nojiri, P. Pfeffer, and W. Zawadzki, *Phys. Rev. B* **55**, 13598 (1997).
60. K. Sugihara, H. Arimoto, and N. Miura, *Physica B* **298**, 195 (2001).
61. G. M. Summers *et al.*, *Phys. Rev. Lett.* **70**, 2150 (1993).
62. C. M. Engelhardt *et al.*, *Surf. Sci.* **305**, 23 (1994).
63. R. J. Nicholas *et al.*, *J. Phys. Soc. Jpn.* **62**, 1267 (1993).
64. N. R. Cooper and J. T. Chalker, *Phys. Rev. Lett.* **72**, 2057 (1994).
65. K. Asano and T. Ando, *J. Phys. Soc. Jpn.* **65**, 1191 (1996).
66. W. Kohn, *Phys. Rev.* **123**, 1242 (1961).
67. R. A. Stradling *et al.*, *Proc. 10th Int. Conf. on Narrow Gap Semiconductors and Related Small Energy Phenomena, Physics and Application* (IPAP Conference Series 2), eds. N. Miura, S. Yamada and S. Takeyama (IPAP, 2001), p. 13.
68. F. F. Fang and P. J. Stiles, *Phys. Rev.* **174**, 823 (1968).
69. D. H. Dickey, E. J. Johnson, and D. M. Larsen, *Phys. Rev. Lett.* **18**, 599 (1967).
70. D. M. Larsen, *Phys. Rev.* **135**, A419 (1964).
71. F. M. Peeters and J. T. Devreese, *Phys. Rev. B* **25**, 7281 (1982).
72. F. M. Peters and J. T. Devreese, *Phys. Rev. B* **34**, 7246 (1986).
73. J. T. Devreese *et al.*, *J. Crystal Growth* **214/215**, 465 (2000).
74. J. Waldman *et al.*, *Phys. Rev. Lett.* **23**, 1033 (1969).
75. C. J. G. M. Langerak *et al.*, *Phys. Rev. B* **38**, 13133 (1988).
76. Y. Imanaka, N. Miura, and H. Kukimoto, *Phys. Rev. B* **49**, 16965 (1994).
77. N. Miura, G. Kido, and S. Chikazumi, in *Physics of Semiconductors*, eds. B. L. H. Wilson (The Institute of Physics, Bristol and London, 1979), p. 1109.
78. N. Miura, G. Kido, and S. Chikazumi, in *Proc. Int. Conf. Application of High Magnetic Fields in Semiconductor Physics*, ed. J. F. Ryan (Oxford, 1978), p. 233.
79. Y. Imanaka *et al.*, *Proc. 15th Int. Conf. on High Magnetic Fields in Semiconductor Physics* (Oxford, 2002).
80. Y. Imanaka, N. Miura, and H. Nojiri, *Physica B* **246-247**, 328 (1998).
81. Y. Imanaka and N. Miura, *Phys. Rev. B* **50**, 14065 (1994).
82. Y. H. Matsuda *et al.*, *Phys. Rev. B* **65**, 115202 (2002).
83. Y. H. Matsuda *et al.*, *Physica B* **256-258**, 565 (1998).
84. J. T. Devreese *et al.*, *Physica B* **298**, 207 (2001).
85. Z. Schlesinger *et al.*, *Phys. Rev. B* **30**, 435 (1984).
86. B. D. McCombe *et al.*, *Phys. Rev. Lett.* **28**, 37 (1972).

87. C. Kallin and B. I. Halperin, *Phys. Rev. B* **31**, 3635 (1985).
88. A. H. MacDonald, *J. Phys. C: Condens. Matter* **18**, 1003 (1985).
89. Y. J. Wang *et al.*, *J. Appl. Phys.* **79**, 8007 (1996).
90. S. Syed *et al.*, *Int. J. Mod. Phys. B* **18**, 3761 (2004).
91. M. A. Zudov *et al.*, *J. Appl. Phys.* **94**, 3271 (2003).
92. D. Some and A. V. Nurmikko, *Phys. Rev. B* **50**, 5783 (1994).
93. D. Some and A. V. Nurmikko, *Phys. Rev. B* **53**, R13295 (1996).
94. X. Wang, R. Srivastava, D. M. Mittleman, and J. Kono, unpublished.
95. M. G. Wright *et al.*, *Semicond. Sci. Technol.* **5**, 438 (1990).
96. N. Ahmed *et al.*, *Semicond. Sci. Technol.* **7**, 357 (1992).
97. J. G. Michels *et al.*, *Semicond. Sci. Technol.* **9**, 198 (1994).
98. J. Cerne *et al.*, *Phys. Rev. Lett.* **77**, 1131 (1996).
99. M. S. Salib *et al.*, *Phys. Rev. Lett.* **77**, 1135 (1996).
100. O. Gywat *et al.*, *Phys. Rev. B* **69**, 205303 (2004).
101. C. J. Meining *et al.*, *Physica E* **26**, 158 (2005).
102. J. Kono *et al.*, *Phys. Rev. Lett.* **79**, 1758 (1997).
103. B. E. Cole *et al.*, *Nature* **410**, 60 (2001).
104. T. Inoshita, *Phys. Rev. B* **61**, 15610 (2000).
105. K. Johnsen and A.-P. Jauho, *Phys. Rev. Lett.* **83**, 1207 (1999).
106. S. Hughes and D. S. Citrin, *Solid State Commun.* **113**, 11 (1999).